

# Structural and Magnetic Properties of High Coercive Al-Substituted Strontium Hexaferrite Nanoparticles

Shahab Torkian<sup>1</sup> · Ali Ghasemi<sup>1</sup> · Reza ShojaRazavi<sup>1</sup> · Majid Tavooosi<sup>1</sup>

Received: 2 January 2016 / Accepted: 2 February 2016 / Published online: 15 February 2016  
© Springer Science+Business Media New York 2016

**Abstract** The aim of this work is to investigate the correlation between replacement of  $\text{Fe}^{3+}$  ions by  $\text{Al}^{3+}$  and structural and magnetic properties of Sr-hexaferrites. To this regard, a simple sol–gel auto-combustion method followed by subsequent heat treatment in air was employed to synthesize nanocrystalline  $\text{SrFe}_{12-x}\text{Al}_x\text{O}_{19}$  ( $0 \leq x \leq 4$ ). X-ray diffraction (XRD), field emission scanning electron microscopy (FE-SEM), Fourier-transform infrared (FT-IR), and vibrating sample magnetometer (VSM) methods were used in order to characterize the produced samples. The results show that the formation of the M-type hexaferrite phase is associated with some  $\alpha\text{-Fe}_2\text{O}_3$  as a secondary phase at low calcination temperature. By increasing the calcination temperature, high-purity hexaferrite phase without any unwanted phases can be formed. The average particle size of the substituted strontium ferrite gradually became smaller by addition of aluminum. The room temperature saturation magnetization values continuously reduced by increasing  $\text{Al}^{3+}$  that is contributed to substitution of  $\text{Fe}^{3+}$  by nonmagnetic ions in the lattice. However, the coercivity initially increases and then decreases with increasing the  $\text{Al}^{3+}$  content. A high coercivity up to 9.1 kOe was obtained for  $\text{SrFe}_{10}\text{Al}_2\text{O}_{19}$  which is much higher than the maximum theoretical value of  $H_C$  for pure  $\text{SrFe}_{12}\text{O}_{19}$  (7.5 kOe).

**Keywords** Strontium hexaferrite · Sol–gel auto-combustion · Al substitution · Magnetic properties

## 1 Introduction

The special properties that are all collected in a group of magnetic materials, namely hexagonal ferrites (Ba, Sr, Pb)  $\text{Fe}_{12}\text{O}_{19}$  with magnetoplumbite structure, have made a lot of requests for this group of materials in recent years. Outstanding features of these ferrites are as follows: low manufacturing cost due to plentiful of their raw materials, stable properties in the ambient, corrosion resistivity, relatively high saturation magnetization, large magnetocrystalline anisotropy and therefore high coercivity, high Curie temperature, comparatively high permeability, and low conductive loss [1–3]. The mentioned magnetic and chemical properties have made hexagonal ferrites popular in every facet of modern life such as telecommunication and microwave devices, magnetic recording and data storage media, electromagnetic wave absorbers, and permanent magnets [4, 5].

The M-phase ferrite is a complex structure of ferrites which allows us to tailor its magnetic parameters and electromagnetic characteristics. In this structure, the oxygen atoms are closed packed with the divalent ( $\text{Ba}^{2+}$ ,  $\text{Sr}^{2+}$ , or  $\text{Pb}^{2+}$ ) and  $\text{Fe}^{3+}$  ions in the interstitial sites. The  $\text{Fe}^{3+}$  ions occupy five different sites that are tetrahedral ( $4f_1$ ), hexahedral, or trigonal bipyramidal (2b) and finally octahedral ( $12k$ ,  $2a$ , and  $4f_2$ ) sites. The spin of  $\text{Fe}^{3+}$  ions in  $12k$ ,  $2a$ , and  $2b$  sites (16 total per unit cell) are up, while the  $\text{Fe}^{3+}$  ions in  $4f_1$  and  $4f_2$  sites (8 total per unit cell) are down spin, which results in a net total of 8 spins up, and therefore, a total moment of  $8 \times 5\mu_B = 40\mu_B$  per unit cell that contains two divalent ions. Because of larger anisotropy constant ( $K_1 = 3.57 \times 10^6 \text{erg/cm}^3$  at  $T = 300 \text{K}$ ), the  $\text{SrFe}_{12}\text{O}_{19}$  is the hardest magnet among the other ferrites [6].

Up to now, a variety of single and multi-cation substitution were used to tune magnetic properties of M-type

✉ Ali Ghasemi  
ali13912001@yahoo.com

<sup>1</sup> Materials Engineering Department, MalekAshtar University of Technology, ShahinShahr, Iran

hexaferrites [7, 8]. Depending on the cation valance and its radius, substituted ion can be replaced with  $\text{Fe}^{3+}$  or  $\text{Sr}^{2+}$  ions. It has been found that substitution of  $\text{Fe}^{3+}$  by divalent-tetravalent metal elements such as Co-Ti, Ni-Ti, Co-Zr, Ni-Zr, Zn-Ti, Co-Sn, Zn-Sn, and Mn-Ti will lead to lowering the coercivity ( $H_C$ ) and also decreases the positive temperature coefficient of coercivity [9]. These magnetic properties are suitable for magnetic recording media, reducing the resonance frequency and broadening the absorbing bands of radar-absorbing materials, etc. [10]. It is well known that doping trivalent elements such as Al, Cr, Ga, etc. in hexaferrites can increase the coercivity and improve their capability for fabrication of permanent magnets. However, due to these substitutions, the saturation magnetization is decreased [1, 11, 12]. In fact, this challenge can be overcome to some extent by controlling the composition and morphology in the produced samples.

Compared to conventional ceramic process for preparation of hexaferrite powders, i.e., physical mixture of oxides, chemical routes including hydrothermal method, the microemulsion process, coprecipitation route, and sol-gel techniques have advantages such as refined particle size, narrow particle size distribution, low crystallization temperature, and high crystallinity [13]. Among all, the sol-gel auto-combustion method has the benefit of process simplicity, low cost, precise control on stoichiometry, nanosized scale of synthesized powders and homogeneity of products that lead to obtain single-phase ferrites after adequate heat treatments [14]. In the current study, the  $\text{SrFe}_{12-x}\text{Al}_x\text{O}_{19}$  ( $x = 0, 1, 2, 3, 4$ ) nanoparticles were synthesized via sol-gel auto-combustion method. The obtained powders were evaluated from phase formation, particle morphology, and magnetic properties. A comparison was made between two calcination temperatures (900 and 1200 °C for 2 h) and various level of  $\text{Al}^{3+}$  substitution on structural and magnetic properties of ferrites.

## 2 Experimental

### 2.1 Synthesis of Substituted Hexaferrite

Ultrafine powders of  $\text{SrFe}_{12-x}\text{Al}_x\text{O}_{19}$  ( $x = 0, 1, 2, 3, 4$ ) were prepared by sol-gel auto-combustion method. The starting materials were of analytical grade (Merck) of iron nitrate ( $\text{Fe}(\text{NO}_3)_3 \cdot 9\text{H}_2\text{O}$ ), strontium nitrate ( $\text{Sr}(\text{NO}_3)_2$ ), aluminum nitrate ( $\text{Al}(\text{NO}_3)_3 \cdot 9\text{H}_2\text{O}$ ), and citric acid ( $\text{C}_6\text{H}_8\text{O}_7 \cdot \text{H}_2\text{O}$ ). According to the  $\text{SrFe}_{12-x}\text{Al}_x\text{O}_{19}$  composition, the stoichiometric amounts of metal nitrate were dissolved in an appropriate amount of de-ionized water by constant stirring on a hotplate at 60 °C to get a clear solution. An aqueous solution of citric acid was slowly

added to metal nitrate solution during stirring to avoid precipitation. The molar ratio of metal ions to citric acid was taken as 1:1.5. After completion of the dissolution, the solution were allowed to cool down to room temperature. Ammonia solution was then added drop by drop to adjust the pH at 6.5. The mixed solution was moved on to a hot plate with continuous stirring at 100 °C. During evaporation, the solution became viscous and finally formed a very viscous brown gel. When all remaining water was released from the mixture; the sticky mass began to bubble. After several minutes, the gel automatically ignited with the formation of large amount of gas and glowingly burnt. The auto-ignition was completed within a minute, yielding lightweight voluminous brown-colored ashes termed as a precursor. The precursor powders were firstly preheated at 450 °C for 1 h, then calcined at 900 and 1200 °C to obtain  $\text{SrFe}_{12-x}\text{Al}_x\text{O}_{19}$  ( $x = 0, 1, 2, 3, 4$ ) hexaferrite phase.

### 2.2 Characterization Methods

X-ray diffraction measurements (XRD) were performed for phase evaluation of the synthesized samples using a Philips diffractometer (MPD-XPET model) with  $\text{Cu K}\alpha$  (1.54 Å) radiation operated at 40 kV and 30 mA (step size of 0.05 and time per step of 0.5 s). FTIR spectroscopy was carried out to evaluate the functional groups which were formed during the sol-gel process using a Bruker TENSOR 27 infrared spectrometer. The IR absorbance was measured in a range between 4000 and 400  $\text{cm}^{-1}$ . The morphology and composition of the substituted hexaferrite nanoparticles were examined using a field emission scanning electron microscope (FE-SEM; Model Mira3-XMU, TESCAN) and energy-dispersive spectroscopy with 15 kV voltage, respectively. The average particle size and its distribution were studied by using microstructural image processing software (MIP 4.1 full; Nahamin Pardazan Asia, Islamic Republic of Iran). For this purpose, more than 200 particles from different micrographs of each samples were evaluated. The Curie temperature of samples was measured by placing a strong magnet above the sample pan during a thermogravimetric essay. As the Curie temperature is crossed, the magnetic properties of the sample will change from ferromagnetic or ferrimagnetic state to paramagnetic state, which is signalled by a sharp apparent weight change of the sample. A vibrating sample magnetometer (VSM; Meghnatis Daghigh Kavir Co, Iran) was used to measure the magnetic properties of the calcined ferrite powders at ambient temperature. The magnetic hysteresis loops were measured at room temperature with maximum applied magnetic field of 15 kOe. The magnetic field sweep rate was 5 Oe/s for all measurements. Saturation magnetization ( $M_S$ ), remanence magnetization

(Mr), and the coercive field ( $H_C$ ) were calculated from the M–H loops.

### 3 Results and Discussion

#### 3.1 Powder XRD Analysis

The XRD patterns of the  $\text{SrFe}_{12-x}\text{Al}_x\text{O}_{19}$  ( $x = 0, 1, 2, 3, 4$ ) powders synthesized by sol–gel combustion method after calcination at 900 and 1200 °C for 2 h are shown in Figs. 1 and 2, respectively. As seen, the main phase consisted in all calcinated samples is  $\text{SrFe}_{12}\text{O}_{19}$  (ICDD card no. 84-1531) which approves the formation of a hexagonal phase. For these samples, a small amount of unwanted antiferromagnetic  $\alpha\text{-Fe}_2\text{O}_3$  (ICDD card no. 79-0007) is observed in the XRD patterns (Fig. 1). The existence of secondary phase indicates the incomplete reaction between  $\text{Fe}^{+3}$  and  $\text{Sr}^{+2}$  under these synthesis conditions. Indeed, local combustion during annealing may lead to formation of undesirable phases that are reported by other researchers too [12, 15]. Elimination of  $\alpha\text{-Fe}_2\text{O}_3$  phase requires longer and higher calcination temperature. This is due to orthorhombic hexahedron crystal structure of  $\alpha\text{-Fe}_2\text{O}_3$  that is difficult to convert into ferrite phase [16]. With increasing the Al concentration in the composition, the amount of  $\alpha\text{-Fe}_2\text{O}_3$  would be decreased. However, the second phase cannot be completely removed unless calcination temperature is raised. In this regard, the XRD patterns of  $\text{SrFe}_{12-x}\text{Al}_x\text{O}_{19}$  ( $x = 0,$

1, 2, 3, 4) calcined samples at 1200 °C for 2 h are presented in Fig. 2. It can be seen that pure hexagonal ferrite with no impurity is obtained after increasing the calcination temperature.

The variation of  $2\theta$  in XRD peaks with substitution of Al in Sr-hexaferrites is shown in the inset of Figs. 1 and 2. For all samples, the XRD peaks are shifted to higher angle region, indicating substitution of aluminum for iron in the hexaferrite structure that decreases its plane distances. In fact, according to Bragg law  $\lambda = 2d \sin \theta$  ( $\lambda$  wavelength of X-rays = 1.5406 Å,  $d$  crystal plane distance, and  $\theta$  angle of diffraction), decreasing the plane distance in crystal structure is associated with moving  $\theta$  towards a higher diffraction angle.

The lattice constants of powders ( $a$  and  $c$ ) were calculated using Miller indices  $h, k, l$ , and  $d$  spacing values of the strong peaks in the XRD patterns using the following equation [17]:

$$\frac{1}{d^2} = \frac{4\sin^2\theta}{\lambda^2} = \frac{4}{3} \left( \frac{h^2 + hk + l^2}{a^2} \right) + \frac{l^2}{c^2} \quad (1)$$

The cell volume ( $V_{\text{cell}}$ ) and X-ray density ( $\rho_{\text{X-ray}}$ ) are calculated using the following formula and listed in Table 1 [18]:

$$V_{\text{cell}} = \frac{\sqrt{3}}{2} a^2 c \quad (2)$$

$$\rho_{\text{X-ray}} = \frac{ZM}{N_A V} \quad (3)$$

**Fig. 1** XRD patterns of produced  $\text{SrFe}_{12-x}\text{Al}_x\text{O}_{19}$  ( $x = 0, 1, 2, 3, 4$ ) calcined at 900 °C for 2 h

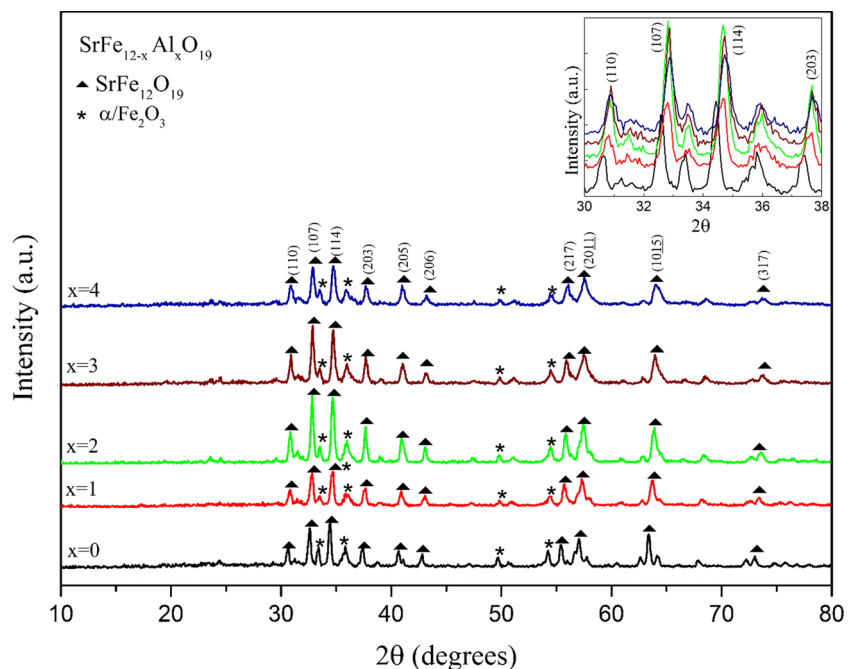
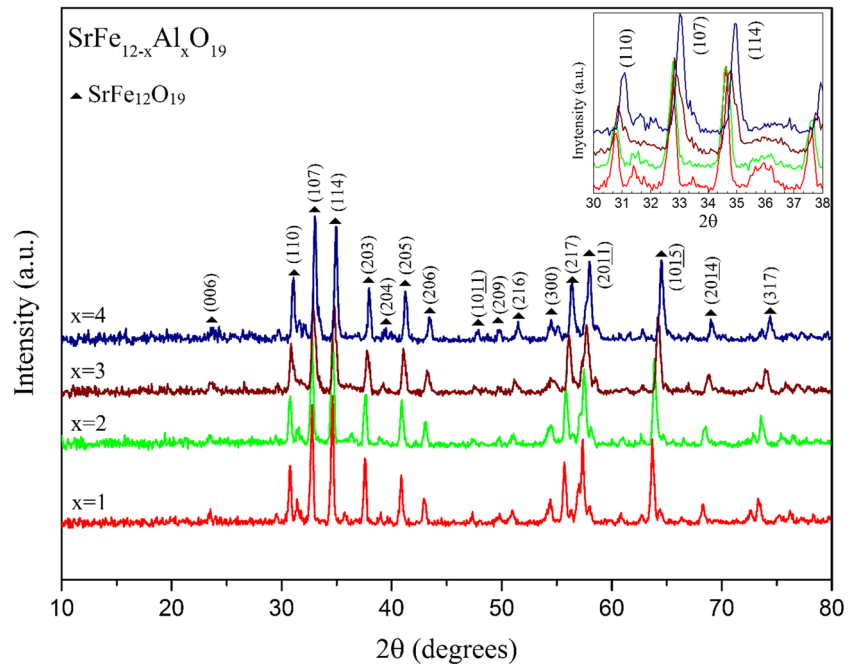


**Fig. 2** XRD patterns of produced  $\text{SrFe}_{12-x}\text{Al}_x\text{O}_{19}$  ( $x = 0, 1, 2, 3, 4$ ) calcined at  $1200^\circ\text{C}$  for 2 h



where  $a$  and  $c$  are the lattice constants as mentioned above,  $Z$  is the number of chemical formula units in a unit cell ( $Z = 2$  for these hexagonal ferrites),  $M$  the molar mass of the samples,  $V$  the unit cell volume, and  $N_A$  Avogadro's number. A negligible rise in the lattice constants occurred by increasing calcination temperatures, but obviously decreased through increasing Al content in the samples. The  $\text{Al}^{3+}$  ion radius ( $0.675 \text{ \AA}$ ) is smaller than that of the  $\text{Fe}^{3+}$  ion ( $0.785 \text{ \AA}$ ) [19]. So introducing Al in the structure results in contraction of the lattice and reducing the unit cell parameters.

The average crystallite size of the samples was calculated by using classical Scherrer relationship as follows [18]:

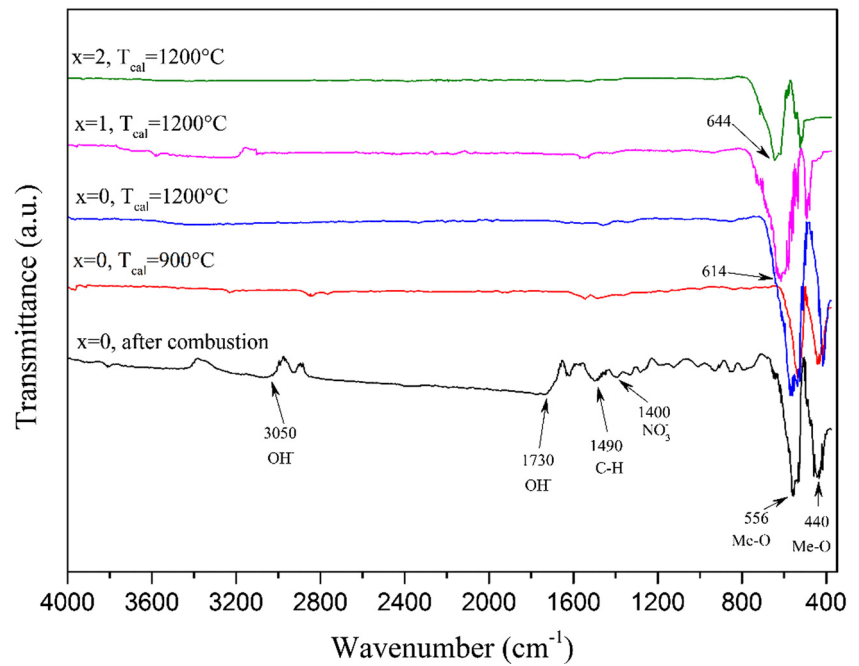
$$D_{(c)} = \frac{0.9\lambda}{\beta \cos \theta} \quad (4)$$

In this equation  $D_c$  is the crystallite size,  $\lambda$  is the X-ray wavelength,  $\beta$  is the FWHM of the relevant diffraction peak, and  $\theta$  is the Bragg angle. As represented in Table 1, the average crystallite size decreases from 80 to 40 and 94 to 51 nm with Al substitution from  $x = 0$  to  $x = 4$  in

**Table 1** Lattice constants  $a$  and  $c$ ,  $c/a$  ratio, cell volume  $V$ , mean crystallite size  $\langle D_c \rangle$ , X-ray density  $\rho_{\text{XRD}}$  and molecular weight  $A$  of the  $\text{SrFe}_{12-x}\text{Al}_x\text{O}_{19}$  ( $x = 0, 1, 2, 3, 4$ ) samples calcined at  $900^\circ\text{C}$  and  $1200^\circ\text{C}$  for 2 h

$x$	$a(\text{\AA})$	$c(\text{\AA})$	$c/a$	$V(\text{\AA}^3)$	$\langle D_c \rangle$ (nm)	$\rho_{\text{XRD}}$ ( $\text{g}/\text{cm}^3$ )	$A$ ( $\text{g}/\text{mol}$ )
$T_{\text{cal}} = 900^\circ\text{C}$							
0	5.84	23.03	3.94	680	80	5.18	1061.74
1	5.81	22.84	3.93	665	70	5.14	1032.9
2	5.80	22.74	3.92	662	65	5.03	1004.05
3	5.79	22.70	3.92	659	47	4.91	975.21
4	5.78	22.61	3.91	660	40	4.76	946.36
$T_{\text{cal}} = 1200^\circ\text{C}$							
0	5.85	22.98	3.93	680	94	5.18	1061.74
1	5.83	22.78	3.91	669	71	5.13	1032.9
2	5.81	22.70	3.90	665	66	5.01	1004.05
3	5.79	22.51	3.88	655	56	4.94	975.21
4	5.76	22.27	3.86	640	51	4.91	946.36

**Fig. 3** FTIR spectra of precursor and calcined  $\text{SrFe}_{12-x}\text{Al}_x\text{O}_{19}$  powders



$\text{SrFe}_{2-x}\text{Al}_x\text{O}_{19}$  for calcination at 900 and 1200 °C, respectively. The obtained crystallite size in this work is smaller as compared to similar investigations reported previously, i.e., 130–165, 140–80, and 300–60 nm for the M-type hexaferrites [13, 20, 21]. The unit cell volume has the same trend and  $V_{\text{cell}}$  value of the substituted ferrite powders were smaller than that of pure  $\text{SrFe}_{12}\text{O}_{19}$ . This reduction in the unit cell volume is accompanied by shortening the diffusion path between nearby grains and consequently smaller grains during calcination would be obtained.

Based on earlier reports in the M-type hexagonal structures, the  $c/a$  ratio is lower than 3.98 [22]. In our samples, the  $c/a$  parameter values are in the range of 3.86–3.94 (Table 1). This value has the acceptable range of M-type hexagonal ferrites.

As expressed in (3), the value of X-ray density is directly related to molecular weight of samples and inversely with volume of the unit cell. Both of these factors are decreased with the increase of concentration of the doped ion. Since the rate of molar weight vanishing is much faster than the cell volume, the X-ray density of samples will be decreased on going to higher amounts of  $\text{Al}^{3+}$  in the composition (Table 1).

### 3.2 Fourier-Transform Infrared Spectroscopy

In order to confirm the complete combustion reaction and formation of the single phase of hexagonal ferrites after calcination, Fourier-transform infrared (FT-IR) spectra of the combusted and calcined powders (samples calcined at 1200 °C) were recorded for  $\text{SrFe}_{12-x}\text{Al}_x\text{O}_{19}$  with  $x = 0, 1, 2$

and the achieved results are shown in Fig. 3. All FT-IR spectra have characteristic absorption bands in the range of 420–540 and 550–600  $\text{cm}^{-1}$  belonging to stretching vibrations of iron-oxygen bond implying hexaferrite formation containing octahedral and tetrahedral sites, respectively [23, 24]. The band observed at 1400  $\text{cm}^{-1}$  for pure  $\text{SrFe}_{12}\text{O}_{19}$  after combustion is attributed to the characteristic band of  $\text{NO}_3^-$ , indicating that the nitrate ions are present in the non-calcined sample. Also, this sample shows an absorption band centered at 3050  $\text{cm}^{-1}$  corresponding to hydrogen bonded O–H stretching. The spectra exhibit an O–H bending band of the  $\text{H}_2\text{O}$  molecules chemically adsorbed to the particle surface around 1730  $\text{cm}^{-1}$  that is diagnostic of the presence of water of hydration. Some weak absorption bands around 1500  $\text{cm}^{-1}$  is observed for the sample calcined at 900 °C, but increasing calcination temperature causes removal of all impurities from ferrite powders. There is an inverse relation between atomic weight and wavenumber in FT-IR spectra [7]. Therefore, increasing substitution of heavier ion ( $M_{\text{Fe}^{3+}} = 56 \text{ g/mol}$ ) by lighter ion ( $M_{\text{Al}^{3+}} = 27 \text{ g/mol}$ ) causes moving characteristic vibration frequency to a higher wavenumber, as represented in Fig. 4. On the other hand, this is proof of the entrance of aluminum into the ferrite lattice.

### 4 Field Emission Electron Microscopy Study

FE-SEM micrographs of  $\text{SrFe}_{12-x}\text{Al}_x\text{O}_{19}$  compounds calcined at 900 and 1200 °C for 2 h have been depicted in Figs. 4 and 5, respectively. It can be seen from Fig. 4a that

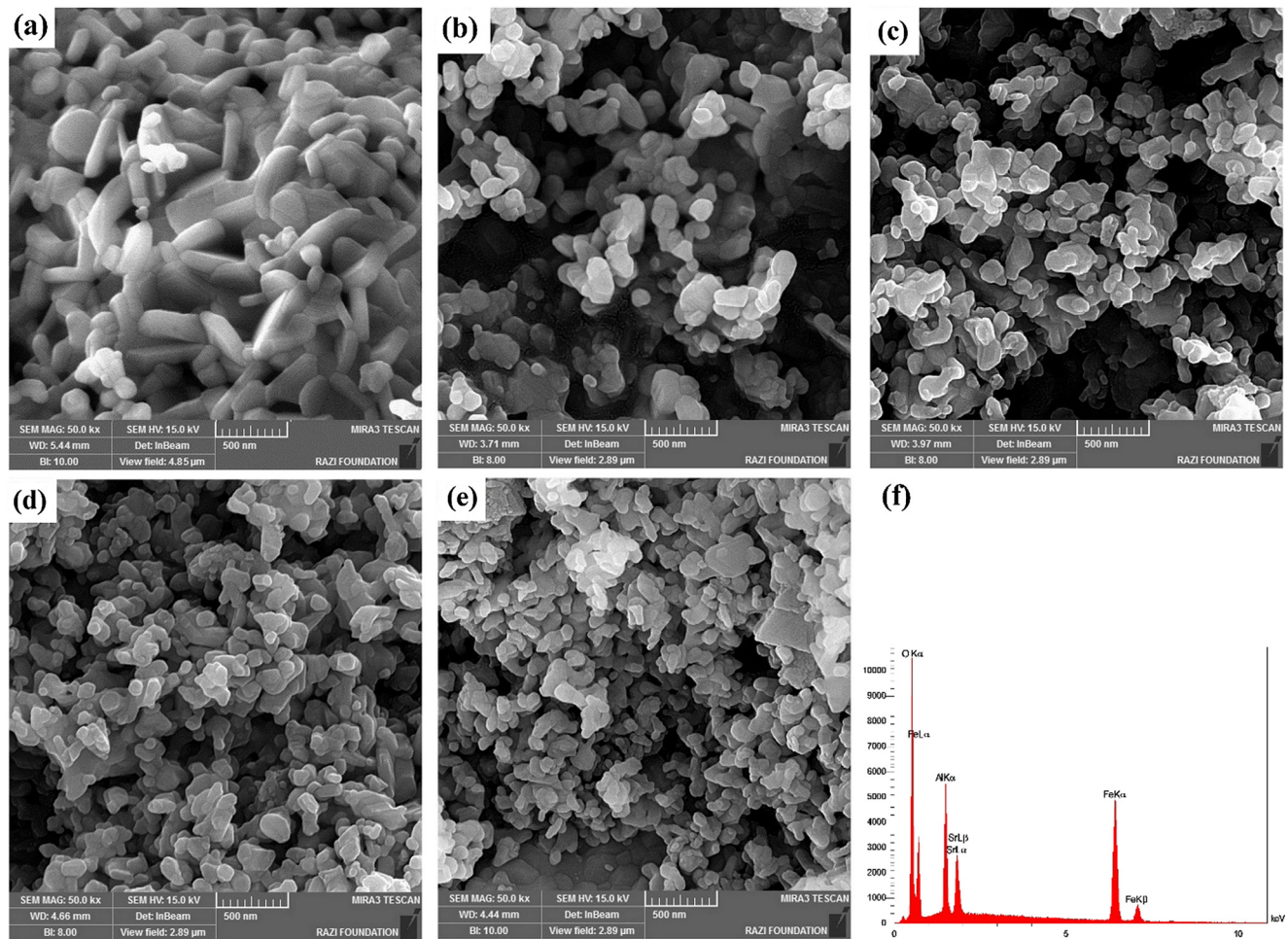


**Fig. 4** FE-SEM micrographs of the  $\text{SrFe}_{12-x}\text{Al}_x\text{O}_{19}$  powders calcined at  $900^\circ\text{C}$  for 2 h with different aluminum contents ( $x$ ): **a**  $x = 0$ , **b**  $x = 1$ , **c**  $x = 2$ , **d**  $x = 3$ , and **e**  $x = 4$ , **f** typical EDS spectra of the  $\text{SrFe}_8\text{Al}_4\text{O}_{19}$  nanoparticles calcined at  $900^\circ\text{C}$  for 2 h

pure strontium hexaferrite calcined at  $900^\circ\text{C}$  has hexagonal platelet-like morphology. By increasing the calcination temperature to  $1200^\circ\text{C}$ , along with the increase in particle size from about  $300$  to  $1\ \mu\text{m}$ , modification in crystallinity of particles has occurred in a way that the particles become distinctly faceted (Fig. 5a). Their crystal formed as a hexagonal bipyramid chopped down parallel to the base. However, the morphology of particles is still not flawless. The nature of self-propagation burning process and lacks of template do not allow  $\text{SrFe}_{12}\text{O}_{19}$  particles to grow completely oriented. The ignition of sample causes generation of large amount of gases during combustion so that high-porous nanoparticles are formed initially, but later, only few of them remain which grow in size at the cost of the smaller ones. Then, a tendency towards agglomeration is observed in the particles due to magneto-dipole interactions between them [25, 26].

Addition of Al cation into the ferrite structure has two results: first, change in morphology, and second, the significant reduction in particle size (Figs. 4b–e and 5b–e).

With increasing Al content, different morphologies such as spherical, pyramidal, and irregular particles appear along with hexagonal platelet-like structures. It is due to entrance of aluminum into the ferrite structure that causes faster growth of some crystalline planes in certain directions. So, particles with special morphologies will be formed. The FE-SEM results reveal that  $\text{Al}^{3+}$  ions play a significant role in grain growth retardation during calcination. In fact, decrease in crystallite size and consequently increase in crystallite boundaries together with presence of aluminum ions on the grain boundaries are responsible for inhibiting the grain growth. As can be seen from Figs. 4 and 5, the particle size in all  $\text{Al}^{3+}$ -doped samples is smaller than the critical size value of  $460\ \text{nm}$  [27] for single-domain magnetic particles. This means that apparently, most of the samples are monodomain which makes them to have an expected improvement in coercivity and we will discuss on it later.

The average particle size of samples is shown in Fig. 6. The distribution of the nanoparticles in most cases is almost

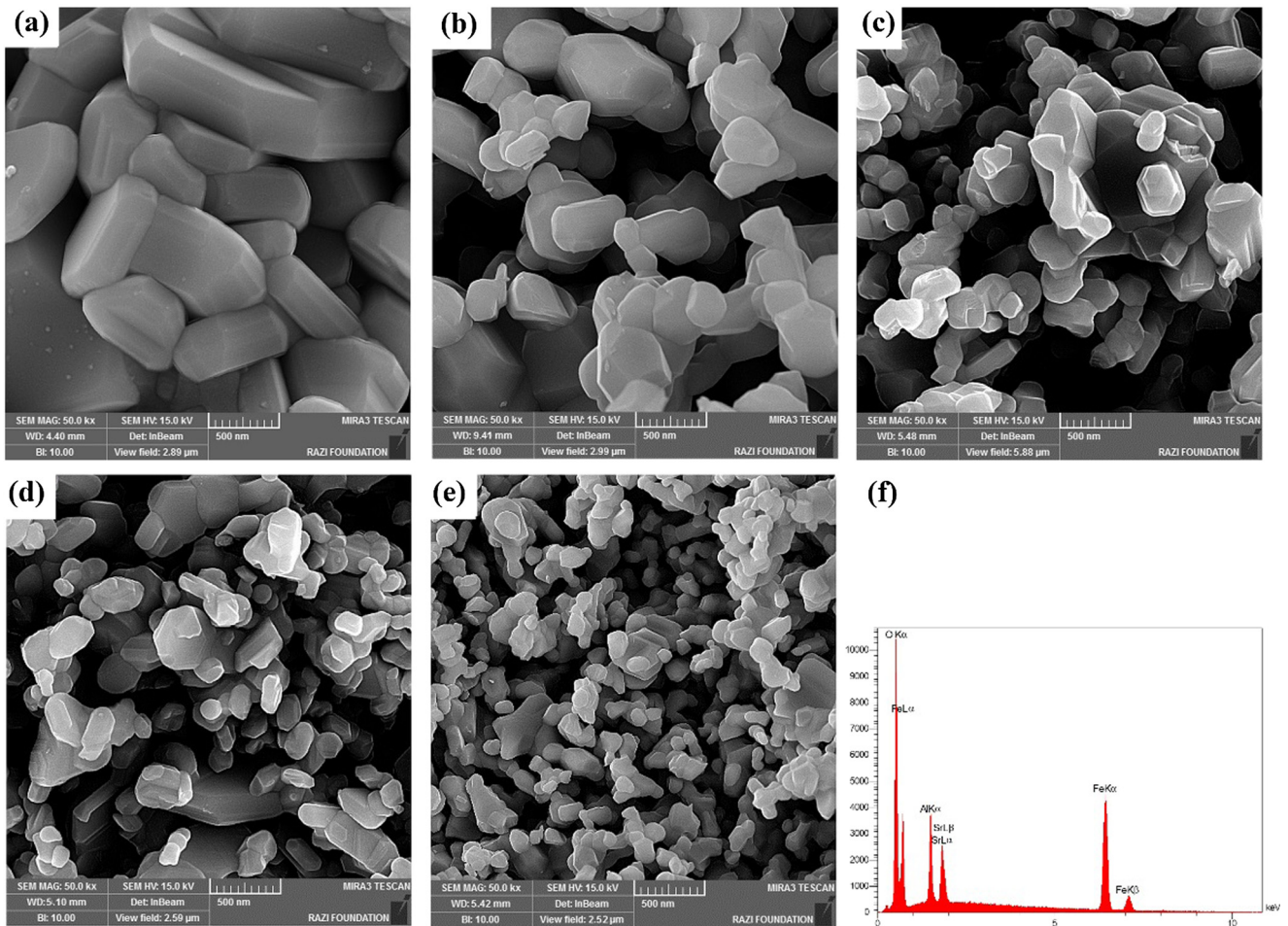


**Fig. 5** FE-SEM micrographs of the  $\text{SrFe}_{12-x}\text{Al}_x\text{O}_{19}$  powders calcined at  $1200\text{ }^\circ\text{C}$  for 2 h with different aluminum contents ( $x$ ): **a**  $x = 0$ , **b**  $x = 1$ , **c**  $x = 2$ , **d**  $x = 3$ , and **e**  $x = 4$ , **f** typical EDS spectra of the  $\text{SrFe}_8\text{Al}_4\text{O}_{19}$  nanoparticles calcined at  $1200\text{ }^\circ\text{C}$  for 2 h

**Fig. 6** Mean particle size obtained from FE-SEM micrographs as a function  $\text{Al}^{3+}$  content for  $\text{SrFe}_{12-x}\text{Al}_x\text{O}_{19}$  powders ( $x = 0, 1, 2, 3, 4$ ) calcined at  $900$  and  $1200\text{ }^\circ\text{C}$  for 2 h. Particle size distribution of  $\text{SrFe}_{11}\text{Al}_1\text{O}_{19}$  powders calcined at  $900\text{ }^\circ\text{C}$  is shown in the *inset* of the figure

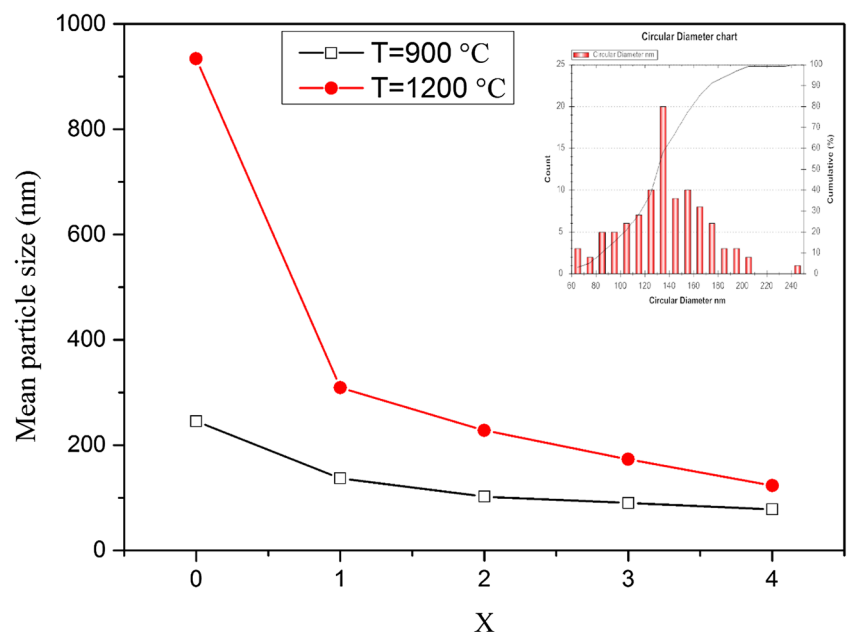


**Table 2** Elemental analysis of the SrFe<sub>12-x</sub>Al<sub>x</sub>O<sub>19</sub> ( $x = 0, 1, 2, 3, 4$ ) samples calcined at 1200 °C for 2 h from EDX analysis

(x)	Elemental Composition (Atomic %)							
	Fe		Sr		O		Al	
	Theo.	Exp.	Theo.	Exp.	Theo.	Exp.	Theo.	Exp.
0	34.2	36.5	3	3.2	62.8	60.3	0	0
1	33.1	33.3	2.7	3.2	61.4	60.3	2.8	3.2
2	31.1	30.2	2.2	3.2	60.4	60.3	6.3	6.3
3	25	27	2	3.2	64	60.3	9	9.5
4	22	23.8	2	3.2	64.2	60.3	11.8	12.7

uniform and has a Gaussian shape that is shown for the SrFe<sub>11</sub>Al<sub>1</sub>O<sub>19</sub> sample in the inset of Fig. 6, for instance. The estimated average particle sizes are approximately within the range of 78–245 and 123–934 nm for SrFe<sub>12-x</sub>Al<sub>x</sub>O<sub>19</sub> ( $x = 0, 1, 2, 3, 4$ ) calcined at 900 and 1200 °C, respectively. A similar trend in crystallite size and particle size of samples can be seen. However, overall average particle size of powders observed via FE-SEM is larger than the crystallite size measured by XRD line broadening due to agglomeration of crystals during calcination and the polycrystalline nature of magnetic ferrites.

## 5 Energy Dispersive Spectroscopy

Energy dispersive spectroscopy (EDS) analysis was used to confirm the chemical composition of the product. Typical EDS elemental analysis spectrum of the SrFe<sub>8</sub>Al<sub>4</sub>O<sub>19</sub> sample synthesized at 900 and 1200 °C is shown in Figs. 4f and 5f, respectively. It was evident that the powders contained mainly Fe, Sr, O, and Al for doped samples. The chemical composition quantification for  $x = 0, 1, 2, 3$ , and 4 is presented in Table 2. Quantitative EDS analysis result showed that the atomic percentage (at %) of metallic ions in the SrFe<sub>12-x</sub>Al<sub>x</sub>O<sub>19</sub> nanoparticles has good agreement with theoretical designed stoichiometry. On the other hand, given that analysis was carried out at different points of each samples and the composition did not show any large variations from spot to spot on the surface, suggesting that the applied process for synthesis SrFe<sub>12-x</sub>Al<sub>x</sub>O<sub>19</sub> nanoparticles is an effective method for the synthesis of hexaferrite material with homogeneity in composition.

## 6 Magnetic Properties

Hysteresis loops of SrFe<sub>12-x</sub>Al<sub>x</sub>O<sub>19</sub> ( $x = 0, 1, 2, 3, 4$ ) calcined at 900 and 1200 °C are shown in Figs. 7 and 8, respectively. The values of saturation magnetization, remanence, squareness ratio, and coercivity of these samples are also listed in Table 3. As seen, synthesized powders show

hard magnetic properties at room temperatures because they have high coercivity and good remanent magnetization. The  $H_C = 5100$  Oe,  $M_S = 59.7$  emu/g, and  $M_r = 33$  emu/g for pure strontium ferrite calcined at 1200 °C for 2 h are in the same range or somewhat larger than those reported by other researchers using similar synthesis methods [4, 11, 28, 29]. With regard to the fact that the maximum applied field was 15 kOe, the saturation state for magnetization was not reached in most samples. However, the maximum recorded value of magnetization was considered as  $M_S$ .

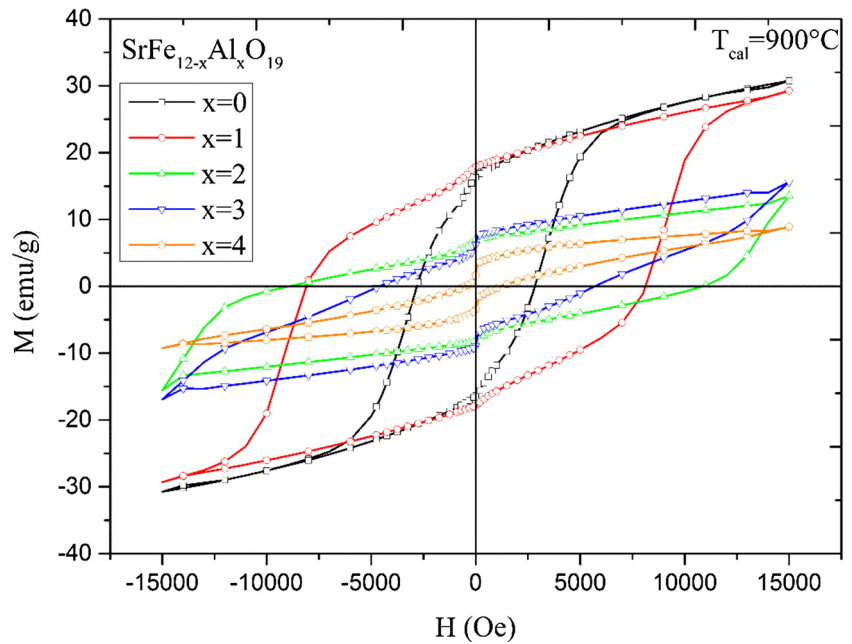
It can be seen that all samples calcined at 1200 °C for 2 h show hysteresis loops of a single-phase magnetic material in shape. But at lower temperature (i.e., 900 °C), some kinks in the loops are observed that it can be attributed to the presence of impurity phases such as  $\alpha$ -Fe<sub>2</sub>O<sub>3</sub> and Al<sub>2</sub>O<sub>3</sub> in the samples. However, it is likely that the presence of these trace phases not be detected by XRD analysis. The existence of nonmagnetic  $\alpha$ -Fe<sub>2</sub>O<sub>3</sub> as the secondary phase in the samples causes degradation of magnetic properties of ferrite. The saturation and remanent magnetization obtained for SrFe<sub>12</sub>O<sub>19</sub> calcined at 1200 °C was about two times

**Table 3** Magnetic properties including saturation magnetization ( $M_S$ ), remanent magnetization ( $M_r$ ), coercivity ( $H_C$ ), squareness ratio ( $M_r/M_S$ ), and magneton number ( $n_B$ ) of SrFe<sub>12-x</sub>Al<sub>x</sub>O<sub>19</sub> ( $x = 0, 1, 2, 3, 4$ ) samples

$x$	$M_S$ (emu/g)	$M_r$ (emu/g)	$M_r/M_S$	$H_C$ (Oe)	$n_B$ ( $\mu_B$ )
$T_{cal} = 900$ °C					
0	30.8	16.3	0.53	2800	5.85
1	29.2	17.8	0.61	8100	5.39
2	15.2	6.8	0.45	9100	2.73
3	13.5	6.2	0.46	6000	2.36
4	8.9	3	0.34	1250	1.51
$T_{cal} = 1200$ °C					
0	59.7	33	0.55	5100	11.34
1	55.5	32.7	0.59	7200	10.26
2	43.4	26	0.60	8100	7.80
3	32.2	21.4	0.66	8450	5.62
4	16.3	8.6	0.53	6000	2.76



**Fig. 7** Hysteresis loops of  $\text{SrFe}_{12-x}\text{Al}_x\text{O}_{19}$  ( $x = 0, 1, 2, 3, 4$ ) samples calcined at  $900^\circ\text{C}$



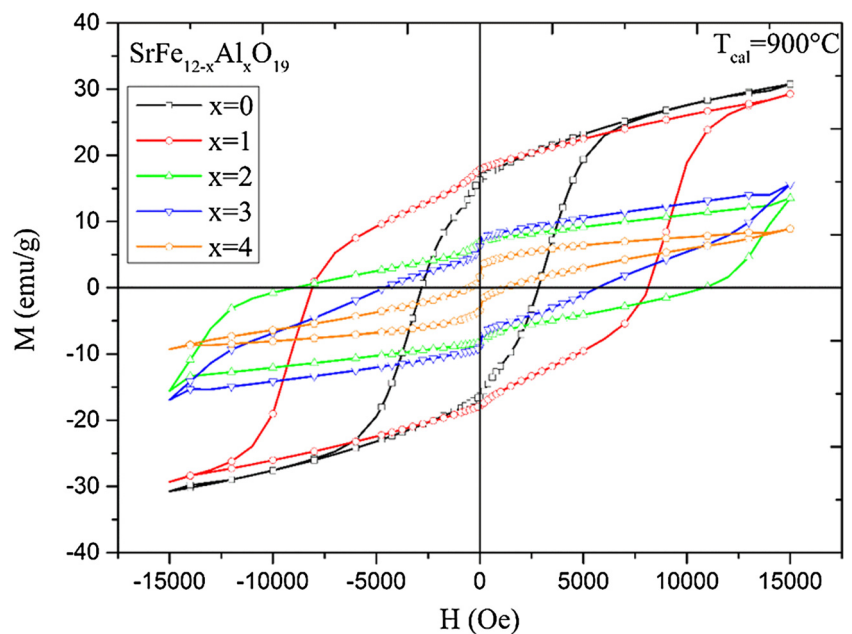
greater than its values for calcination at  $900^\circ\text{C}$  (Table 3). The content of  $\text{SrFe}_{12}\text{O}_{19}$  gradually increases, as well as the crystallinity and homogeneity of microstructure, and that of the  $\alpha\text{-Fe}_2\text{O}_3$  decreases with increasing calcination temperature. Therefore, with increasing calcination temperature, the coercivity, saturation magnetization, and remanence will be increased, as shown in Figs. 7 and 8. The squareness ratio  $M_r/M_s$  of approximately 0.5 for all compositions (Table 3) suggests that Sr-hexaferrite are randomly oriented domain particles [30].

The magnetic properties are evidently altered by the addition of  $\text{Al}^{3+}$  ion. Increase of  $\text{Al}^{3+}$  leads to decline in

magnetization, but the coercivity rises to large values up to  $x = 3$  and then decreases for  $x = 4$ . Samples with  $\text{Al}^{3+}$  content  $x = 2$  calcined at  $900^\circ\text{C}$  and with  $\text{Al}^{3+}$  content  $x = 3$  calcined at  $1200^\circ\text{C}$  show maximum coercivity equal to 9.1 and 8.45 kOe, respectively. These values of  $H_C$  are greater than the maximum value of coercivity for single-crystal strontium ferrite (6.7 kOe) and even its maximum theoretical value (7.5 kOe) [6].

In order to justify the variation of magnetic properties upon doping  $\text{Al}^{3+}$ , the placement of doped cation at different sites in the hexagonal structure of the ferrite should be considered. In M-type hexagonal ferrites 24  $\text{Fe}^{3+}$  ions

**Fig. 8** Hysteresis loops of  $\text{SrFe}_{12-x}\text{Al}_x\text{O}_{19}$  ( $x = 0, 1, 2, 3, 4$ ) samples calcined at  $1200^\circ\text{C}$



are distributed over five distinct sites: three octahedral sites (12k, 2a, and 4f<sub>2</sub>), one tetrahedral site (4f<sub>1</sub>) and one bipyramidal site (2b). This ferrimagnetic structure includes four parallel (4f<sub>1</sub> and 4f<sub>2</sub>) and eight antiparallel (12k, 2a, and 2b) spins which are coupled by super exchange interactions mediated by O<sup>2-</sup> ions. So there is a net total of 4 spin ups and the total magnetic moment per unit formula will be equal to  $4 \times 5\mu_B = 20\mu_B$  [31]. It has been reported [4, 32], when aluminum incorporates into M-type hexaferrite, at level of doping below  $x = 3$ , the octahedral sites (mainly 12 k) and at higher level of doping ( $x > 4$ ) the hexahedral site (2b), which all have upward spins, will be occupied. The nonmagnetic Al<sup>3+</sup> ions with zero magnetic moment replace with Fe<sup>3+</sup> ions from the sites having spins in upward direction, which have  $5\mu_B$  magnetic moment. As a result, a reduction in the saturation magnetization and remanence of the synthesized materials is reasonable (Table 3). From the saturation magnetization data, the magneton number per unit formula ( $n_B$ ) is calculable using the following equation [33]:

$$n_B = \frac{A \times M_S}{d \times N_a \times \mu_B} \quad (5)$$

In this equation,  $A$  is molecular weight,  $M_S$  is saturation magnetization in electromagnetic unit per cubic centimeter,  $d$  is density of sample,  $N_a$  is Avogadro's number, and  $\mu_B$  is Bohr magneton  $= 9.27 \times 10^{-21}$  erg/Oe. The values of magneton number are listed in Table 3. It is clear that  $n_B$  decreases with increase in Al content. As the magnetic moment and saturation magnetization are directly related to each other, decrease in the saturation magnetization upon Al<sup>3+</sup> doping leads to a decrease in the magnetic moment that agrees with the above discussion.

In addition to magnetic dilution, decrease in superexchange interaction between Fe<sub>A</sub><sup>3+</sup>–O–Fe<sub>B</sub><sup>3+</sup> due to replacement of Fe<sup>3+</sup> with paramagnetic Al<sup>3+</sup> ion is another reason for reduction of magnetization value [34]. Size reduction and nanocrystalline nature of synthesized powders will make some defects on the surface of nanoparticles. In this condition, decrease in the exchange interaction and surface defects causes spin canting or non-collinear magnetic ordering on the nanoparticles surface [35]. Thus, magnetic ion spins align in different angles with respect to easy axis of magnetization ( $c$ -axis for  $M$  structure ferrites). When canted spin occurred, it gives suppressions of exchange interaction strength and promotes lower  $M_S$ . The above factors result in magnetization reduction of samples with doping Al<sup>3+</sup>, as evident from Table 3.

The coercivity of samples can be obtained from hysteresis loops at a point where the magnetization vanishes to zero after reversing the magnetic field from saturation state. The  $H_C$  values for non-doped SrFe<sub>12</sub>O<sub>19</sub> calcined at 900 °C

was 2.8 kOe. Increasing the calcination temperature to 1200 °C results in rising the coercivity up to 5.1 kOe. The low value of coercivity for sample calcined at lower temperature is due to the non-complete formation of hexagonal ferrite as previously confirmed by structural analysis, low crystalline anisotropy, and crystal imperfections. Improvement of phase formation during high calcination temperature increases the  $H_C$  value to 5.1 kOe. This value is lower than that of single-domain SrFe<sub>12</sub>O<sub>19</sub> with  $H_C \sim 6.3$  kOe which was made from coprecipitated salts and also lower than maximum theoretical value of strontium ferrite coercivity equal to 7.5 kOe [6]. The formation of multi-domain due to grain growth during high calcination temperature ( $D_p \sim 0.9 \mu m$ ) and easy movement of the domain walls and also a high degree of aggregation in the samples results in the decrease of the coercivity.

It can be seen from Figs. 7 and 8 that the Al<sup>3+</sup> ion has a significant increase effect on the coercivity of SrFe<sub>12-x</sub>Al<sub>x</sub>O<sub>19</sub>. According to the  $H_C$  values listed in Table 3, it increases for  $x$  going from 0 to 2 and 3, for calcination at 900 and 1200 °C, respectively. Then, it decreases with further Al<sup>3+</sup> doping. This behavior is contrary to what occurred for magnetization trend in response to Al<sup>3+</sup> doping. As compared to pure strontium ferrite, the 225 and 65.7 % enhancement of  $H_C$  was obtained for SrFe<sub>10</sub>Al<sub>2</sub>O<sub>19</sub> and SrFe<sub>9</sub>Al<sub>3</sub>O<sub>19</sub> compounds calcined at 900 and 1200 °C, respectively. For these two samples, the reduction of saturation magnetization was about 50 %, whereas for the sample with  $x = 2$  calcined at 1200 °C, only 27.3 % decrease in the saturation magnetization against 58.8 % increase of coercivity was obtained. To investigate this behavior, we should consider the factors affecting the coercivity of ferrites such as the particle size and shape, size distribution, lattice defects, interface structure, presence of impurity phases, and various magnetic anisotropies of material [11, 36]. Grain size and magnetocrystalline anisotropy are the most influential factors among the others. The optimum value of coercivity is obtained when the grain size be smaller than the magnetic domain size. The maximum values of  $H_C$  for random array of monodomain particles is given by the Stoner-Wohlfarth model of magnetization [37]:

$$H_C = 0.48[(2k_1)/M_S - NM_S] \quad (6)$$

where inside the bracket, the first term stands for the magnetocrystalline anisotropy field  $H_A$  with  $K_1$  is the first-order magnetocrystalline anisotropy constant and the second one represents the demagnetization field with  $N$  the demagnetization coefficient of particles. In (6), we used experimental data for saturation magnetization of SrFe<sub>12-x</sub>Al<sub>x</sub>O<sub>19</sub> described by Wohlfarth [38]:

$$M_S(x) = M_S(x=0)(1 - \frac{x}{4}) \quad (7)$$

**Table 4** Single-domain particle size ( $D_{crit}$ ) calculated from (9) for  $SrFe_{12-x}Al_xO_{19}$  ( $x = 0, 1, 2, 3, 4$ ) calcined at 1200 °C Magnetocrystalline anisotropy constant ( $K_1$ ) from (8) is used in  $D_{crit}$  calculation.

Domain wall density energy from (10). Mean particle size  $D_p$  from FE-SEM images are listed for comparison with  $D_{crit}$

$x$	Lattice constant $a(\text{Å})$	$T_c (K) \pm 2K$	$M_s (Gs)$	$K_1 \times 10^6 (\text{erg/cm}^3)$	$\sigma_w (\text{erg/cm}^2)$	$D_{crit} (\text{nm})$	$D_p (\text{nm})$
0	5.85	724	309.2	3.57	3.50	527	934
1	5.82	678	284.7	2.97	3.09	546	309
2	5.81	608	217.4	2.38	2.62	795	228
3	5.79	591	159.1	1.78	2.24	1267	173
4	5.76	576	80.1	1.19	1.81	4048	123

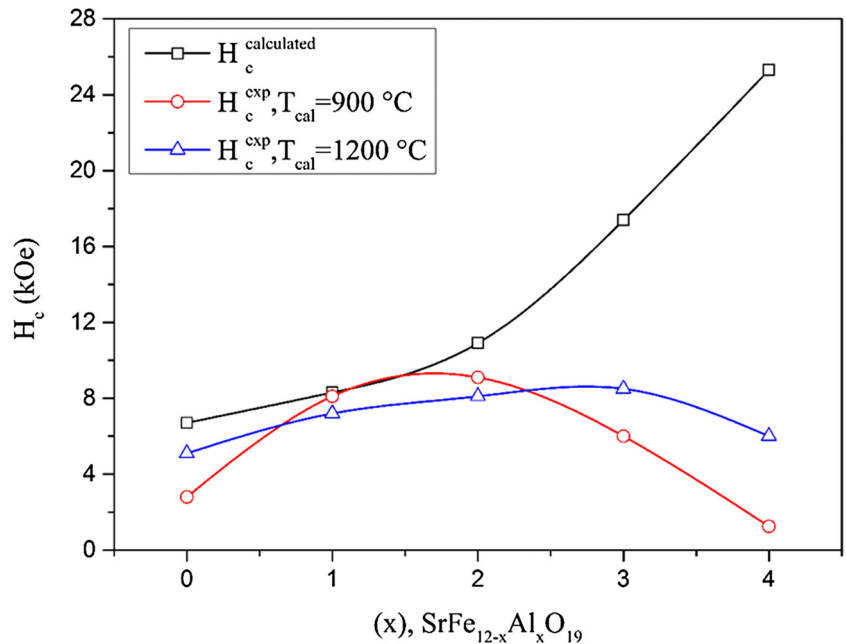
Based on previous reports, the saturation magnetization of  $SrFe_{12}O_{19}$  was taken as  $M_S = 380 \text{ emu/cm}^3$  at room temperature. The value of the first magnetocrystalline anisotropy which was used in (6) for coercivity calculation is obtained by this relation [39]:

$$k_1(x)/k_1(0) = (24 - 4x)/24 \tag{8}$$

This equation suggests for Al-substituted strontium ferrite magnetocrystalline anisotropy is dependent on composition and assumes  $K_1(x)$  is proportional to the total number of moments per cell. This assumption implies that the magnetocrystalline coupling has about the same strength for all of the five crystallographic sites. Taking into account  $K_1(0) = 3.57 \times 10^6 \text{ erg/cm}^3$  for pure strontium hexaferrite [40], the values of  $K_1(x)$  for bulk  $SrFe_{12-x}Al_xO_{19}$  were calculated based on (8) and are presented in Table 4. Finally, from the calculated  $K_1(x)$  and  $M_S(x)$  values, the maximum coercivity  $H_C^{calc}$  obtained using (6) and are plotted in Fig. 9 as a function of aluminum content. The experimental values of  $H_C$  for fabricated ferrites are

also shown in this figure. It is clear that  $H_C$  increases with increase of  $Al^{3+}$  ion in the compound. The behavior of calculated  $H_C$  is different from experimental results as it increases continuously with  $x$ , but for fabricated samples, its value initially increases and then decreases with the  $Al^{3+}$  ion content. On the other hand the difference between calculated and measured data becomes remarkable after  $x = 2$ . The reason of this occurrence can be found in the change of magnetocrystalline anisotropy and particle size in the real state. According to (6), the coercivity has a direct relationship with  $K_1$  and inversely related to  $M_S$ . Based on Mossbauer spectroscopy, it has been reported before when the  $Al^{3+}$  ion content is under  $x = 2$ , the octahedral and tetrahedral sites are mainly occupied [41]. In this condition a weak decrease of the anisotropy constant will be caused due to substituted ion. But the  $M_S$  value vanishes rapidly. So an uptrend in the  $H_C$  is observed. On the other hand, when the substituted  $Al^{3+}$  ion content  $x$  is over 2.0, a significant decrease in anisotropy constant results from occupation of hexahedral sites by  $Al^{3+}$  ions. Thus the decrease rate of  $K_1$

**Fig. 9** Coercivity  $H_C^{exp}$  of the  $SrFe_{12-x}Al_xO_{19}$  ( $x = 0, 1, 2, 3, 4$ ) samples calcined at 900 and 1200 °C as a function of  $Al^{3+}$  content. The calculated coercivity values  $H_C^{calc}$  are also shown



overcome the  $M_S$  reduction and the upward trend of coercivity will be suppressed. In the theoretical calculation of  $K_1$  used in (6), it was supposed that the magnetocrystalline coupling strength is the same for all of the five crystallographic sites. While in practice, replacement of  $\text{Fe}^{3+}$  ions with non-magnetic  $\text{Al}^{3+}$  breaks down the magnetic collinearity of strontium ferrite due to repression of the strong tetragonal and octahedral exchange interaction.

As mentioned above, another important factor that has a major effect on coercivity is the particle size. When particle size is larger than a critical size, multidomain structure will be formed. In this case, the magnetization process can take place by domain wall displacement and  $H_C$  will be small. By decreasing the particle size, single domains develop. Elimination of domain walls and demagnetization process by coherent rotation of spins can lead to attainment of maximum value of coercivity. With a further decrease in particle size below a critical diameter, the coercivity becomes zero and such particles become superparamagnetic [42]. So it will be useful to calculate the critical size of a single-domain particle. As suggested by Kittel [43], the critical particle size  $D_{\text{crit}}$  for a spherical particle at which a single domain state can be realized is as follows:

$$D_{\text{crit}} = \frac{9\sigma_w}{2\pi M_S^2} \quad (9)$$

and

$$\sigma_w = \sqrt{\frac{2k_B T_c |k_1|}{a}} \quad (10)$$

where  $M_S$  is the saturation magnetization,  $\sigma_w$  is the surface energy per unit wall area,  $k_B$  is the Boltzmann constant,  $T_c$  is the Curie temperature as measured based on what was described in the experimental section,  $|k_1|$  is the magnetocrystalline anisotropy constant and  $a$  is the lattice constant as obtained from XRD data. These data are listed in Table 4. For  $D_p > D_{\text{crit}}$ , the particles have multi-domain structures, while for  $D_p < D_{\text{crit}}$  the particles are in monodomain state. It can be seen that for all samples  $D_p < D_{\text{crit}}$  except for samples calcined at 1200 °C. Also by increasing  $\text{Al}^{3+}$  substitution, the critical size increases strongly from submicron to micron sizes whereas the particle sizes of the samples approach nanometer scale. Therefore upon doping  $\text{Al}^{3+}$ , the particle sizes are decreased and become smaller than critical singledomain size. This implies the formation of monodomain particles that prevents the domain wall motion, which causes an increase in the coercivity. Furthermore,  $H_C$  reduces at higher  $\text{Al}^{3+}$  content for  $x = 4$ . This reduction is primarily due to considerable decrease in magnetocrystalline anisotropy constant. Another reason for the reduction of  $H_C$  at higher level of doping can be attributed to very small size character of particles. It is clear from

Table 4 that for samples with  $x = 4$  calcined at 1200 °C, the average particle size is more than 30 times smaller than  $D_C$ . Based on the above discussion, when the particle size becomes much smaller than the critical size, the coercivity will be reduced.

The Curie temperature of samples is decreased with  $\text{Al}^{3+}$  ion substitution as presented in Table 4. As mentioned above, when the non-magnetic  $\text{Al}^{3+}$  ions enter the lattice, some super-exchange interactions will be suppressed, which causes the magnetic collinearity break down. As the  $T_C$  is determined by the overall strength of the exchange interactions, it can be argued that the weakening of the exchange interaction and spin canting on the surface of nanoparticles is responsible for the decrease of  $T_C$  values.

## 7 Conclusion

A series of submicron and nanometer scale of Al-doped ferrite powders of the composition  $\text{SrFe}_{12-x}\text{Al}_x\text{O}_{19}$  ( $x = 0, 1, 2, 3, 4$ ) have been successfully synthesized via sol-gel auto-combustion method followed by calcining at two different temperatures for 2 h. XRD patterns confirmed the formation of pure M-type ferrite in all samples calcined at 1200 °C; however some secondary phases such as  $\alpha\text{-Fe}_2\text{O}_3$  exist for samples calcined at lower temperature, i.e. 900 °C. The average grain size reduces from 80 to 40 and 94 to 51 nm with  $\text{Al}^{3+}$  substitution from  $x = 0$  to  $x = 4$  for calcination at 900 and 1200 °C, respectively. The FE-SEM micrographs of compounds showed substitution of  $\text{Fe}^{3+}$  by  $\text{Al}^{3+}$  reduces the particle size from submicron to nanoscale range. The magnetic data reveal that pure  $\text{SrFe}_{12}\text{O}_{19}$  calcined at 1200 °C for 2 h has a good characteristic of hard magnetic material with saturation magnetization of 59.7 emu/g, remanence of 33 emu/g and coercivity of 5.1 kOe. Addition of  $\text{Al}^{3+}$  ion enhances the coercivity, but it reduces the saturation of magnetization. However, for samples with  $x = 2$  calcined at 1200 °C, only 27.3 % decrease in the saturation magnetization against 58.8 % increase of coercivity was obtained. The maximum  $H_C$  of 9.1 kOe was achieved for  $\text{SrFe}_{10}\text{Al}_2\text{O}_{19}$  that is 21.3 % larger than the maximum theoretical value of coercivity for pure strontium ferrite (7.5 kOe).

## References

1. Ashiq, M.N., Javed Iqbal, M., Hussain Gul, I.: Effect of Al-Cr doping on the structural, magnetic and dielectric properties of strontium hexaferrite nanomaterials. *J. Magn. Magn. Mater.* **323**(3–4), 259–263 (2011)
2. Wang, H.Z., Yao, B., Xu, Y., He, Q., Wen, G.H., Long, S.W., Fan, J., Li, G.D., Shan, L., Liu, B., Jiang, L.N., Gao, L.L.: Improvement

- of the coercivity of strontium hexaferrite induced by substitution of  $Al^{3+}$  ions for  $Fe^{3+}$  ions. *J. Alloys Compd.* **537**, 43–49 (2012)
3. Ghasemi, A.: Tuning static and high frequency magnetic properties of  $SrFe_{12-x}(Mn_{0.5}Co_{0.5}Ti)_{x/2}O_{19}$  nanoparticles and thin films via chemical control. *J. Magn. Magn. Mater.* **378**, 340–344 (2015)
  4. Luo, H., Rai, B.K., Mishra, S.R., Nguyen, V.V., Liu, J.P.: Physical and magnetic properties of highly aluminum doped strontium ferrite nanoparticles prepared by auto-combustion route. *J. Magn. Magn. Mater.* **324**(17), 2602–2608 (2012)
  5. Chawla, S.K., Mudsainiyani, R.K., Meena, S.S., Yusuf, S.M.: Sol-gel synthesis, structural and magnetic properties of nanoscale M-type barium hexaferrites  $BaCo_xZr_xFe_{(12-2x)}O_{19}$ . *J. Magn. Magn. Mater.* **350**, 23–29 (2014)
  6. Pullar, R.C.: Hexagonal ferrites: A review of the synthesis, properties and applications of hexaferrite ceramics. *Prog. Mater. Sci.* **57**(7), 1191–1334 (2012)
  7. Liu, M., Shen, X., Song, F., Xiang, J., Meng, X.: Microstructure and magnetic properties of electrospun one-dimensional  $Al^{3+}$ -substituted  $SrFe_{12}O_{19}$  nanofibers. *J. Solid State Chem.* **184**(4), 871–876 (2011)
  8. Chawla, S.K., Meena, S.S., Kaur, P., Mudsainiyani, R.K., Yusuf, S.M.: Effect of site preferences on structural and magnetic switching properties of CO-Zr doped strontium hexaferrite  $SrCo_xZr_xFe_{(12-2x)}O_{19}$ . *J. Magn. Magn. Mater.* **378**, 84–91 (2015)
  9. Wang, J.F., Ponton, C.B., Harris, I.R.: A study of the magnetic properties of hydrothermally synthesised Sr hexaferrite with Sm substitution. *J. Magn. Magn. Mater.* **234**(2), 233–240 (2001)
  10. Ghasemi, A., Liu, X., Morisako, A.: Magnetic and microwave absorption properties of  $BaFe_{12-x}(Mn_{0.5}Cu_{0.5}Zr)_{x/2}O_{19}$  synthesized by sol-gel processing. *J. Magn. Magn. Mater.* **316**(2), e105–e108 (2007)
  11. Rai, B.K., Mishra, S.R., Nguyen, V.V., Liu, J.P.: Synthesis and characterization of high coercivity rare-earth ion doped  $Sr_{0.9}RE_{0.1}Fe_{10}Al_2O_{19}$  (RE: Y, La, Ce, Pr, Nd, Sm, and Gd). *J. Alloys Compd.* **550**, 198–203 (2013)
  12. Hojjati Najafabadi, A., Mozaffarinia, R., Ghasemi, A.: Microstructural characteristics and magnetic properties of Al-substituted barium hexaferrite nanoparticles synthesized by auto-combustion sol-gel processing. *J. Supercond. Nov. Magn.* **28**(9), 2821–2830 (2015)
  13. He, H.Y., Huang, J.F., Cao, L.Y., He, Z., Shen, Q.: Magnetic and microwave-absorbing properties of  $SrAl_4Fe_8O_{19}$  powders synthesized by coprecipitation and citric-combustion methods. *Bull. Mater. Sci.* **34**(3), 463–468 (2011)
  14. Yang, X., Li, Q., Zhao, J., Li, B., Wang, Y.: Preparation and magnetic properties of controllable-morphologies nano- $SrFe_{12}O_{19}$  particles prepared by sol-gel self-propagation synthesis. *J. Alloys Compd.* **475**(1–2), 312–315 (2009)
  15. Fu, Y.-P., Lin, C.-H., Pan, K.-Y.: Strontium hexaferrite powders prepared by a microwave-induced combustion process and some of their properties. *J. Alloys Compd.* **349**(1–2), 228–231 (2003)
  16. Qiu, J., Liang, L., Gu, M.: Nanocrystalline structure and magnetic properties of barium ferrite particles prepared via glycine as a fuel. *Mater. Sci. Eng. A* **393**(1–2), 361–365 (2005)
  17. Narang, S.B., Singh, A., Singh, K.: High frequency dielectric behavior of rare earth substituted Sr-M hexaferrite. *J. Ceram. Process. Res.* **8**(5), 347 (2007)
  18. Cullity, B.D., Stock, S.R.: *Elements of X-ray Diffraction*, 3rd edn. Prentice Hall (2001)
  19. Shannon, R.T.: Revised effective ionic radii and systematic studies of interatomic distances in halides and chalcogenides. *Acta Crystallogr., Sect. A: Cryst. Phys., Diffr., Theor. Gen. Crystallogr.* **32**(5), 751–767 (1976)
  20. Nga, T.T.V., Duong, N.P., Hien, T.D.: Composition and magnetic studies of ultrafine Al-substituted Sr hexaferrite particles prepared by citrate sol-gel method. *J. Magn. Magn. Mater.* **324**(6), 1141–1146 (2012)
  21. Mu, G., Chen, N., Pan, X., Shen, H., Gu, M.: Preparation and microwave absorption properties of barium ferrite nanorods. *Mater. Lett.* **62**(6), 840–842 (2008)
  22. Wagner, T.: Preparation and crystal structure analysis of magnetoplumbite-type  $BaGa_{12}O_{19}$ . *J. Solid State Chem.* **136**(1), 120–124 (1998)
  23. Khademi, F., Poorbafrani, A., Kameli, P., Salamati, H.: Structural, magnetic and microwave properties of Eu-doped barium hexaferrite powders. *J. Supercond. Nov. Magn.* **25**(2), 525–531 (2012)
  24. Singhal, S., Namgyal, T., Singh, J., Chandra, K., Bansal, S.: A comparative study on the magnetic properties of  $MFe_{12}O_{19}$  and  $MAFe_{11}O_{19}$  (M = Sr, Ba and Pb) hexaferrites with different morphologies. *Ceram. Int.* **37**(6), 1833–1837 (2011)
  25. Liu, M., Song, F., Shen, X., Zhu, Y.: Effects of strontium silicate on structure and magnetic properties of electrospun strontium ferrite nanofibers. *J. Sol-Gel Sci. Technol.* **56**(1), 39–46 (2010). doi:10.1007/s10971-010-2270-1
  26. Ghasemi, A., Ekhlesi, S., Mousavinia, M.: Effect of Cr and Al substitution cations on the structural and magnetic properties of  $Ni_{0.6}Zn_{0.4}Fe_{2-x}Cr_{x/2}Al_{x/2}O_4$  nanoparticles synthesized using the sol-gel auto-combustion method. *J. Magn. Magn. Mater.* **354**, 136–145 (2014)
  27. Zi, Z., Sun, Y., Zhu, X., Yang, Z., Song, W.: Structural and magnetic properties of  $SrFe_{12}O_{19}$  hexaferrite synthesized by a modified chemical co-precipitation method. *J. Magn. Magn. Mater.* **320**(21), 2746–2751 (2008)
  28. Herme, C., Bercoff, P., Jacobo, S.: Nd-Co substituted strontium hexaferrite powders with enhanced coercivity. *Mater. Res. Bull.* **47**(11), 3881–3887 (2012)
  29. Sahu, R.K., Mohanta, O., Pramanik, A.: XPS study on the correlation of magnetic properties and site occupancy of Al doped  $SrFe_{12}O_{19}$ . *J. Alloys Compd.* **532**, 114–120 (2012)
  30. Went, J., Rathenau, G., Gorter, E., Van Oosterhout, G.: Ferroxidure, a class of new permanent magnet materials. *Philips Tech. Rev.* **13**(194), 1951 (1952)
  31. Özgür, Ü., Alivov, Y., Morkoç, H.: Microwave ferrites, part 1: fundamental properties. *J. Mater. Sci. Mater. Electron.* **20**(9), 789–834 (2009)
  32. Albanese, G.: Mössbauer investigation of aluminium substituted barium hexaferrite in the paramagnetic state. *J. Magn. Magn. Mater.* **147**(3), 421–426 (1995)
  33. Goldman, A. *Modern Ferrite Technology*, 2nd edn. Springer, US (2006)
  34. Albanese, G., Carbuicchio, M., Deriu, A.: Temperature dependence of the sublattice magnetizations in Al- and Ga-substituted M-type hexagonal ferrites. *Phys. Status Solidi A* **23**(2), 351–358 (1974)
  35. Liu, X., Zhong, W., Yang, S., Yu, Z., Gu, B., Du, Y.: Influences of La 3+ substitution on the structure and magnetic properties of M-type strontium ferrites. *J. Magn. Magn. Mater.* **238**(2), 207–214 (2002)
  36. Bottoni, G., Candolfo, D., Cecchetti, A., Giarda, L., Masoli, F.: The grinding effects on magnetization processes in Ba ferrite powders by rotational hysteresis. *Phys. Status Solidi A* **32**(1), K47–K50 (1975)
  37. Stoner, E.C., Wohlfarth, E.: A mechanism of magnetic hysteresis in heterogeneous alloys. *Phil. Trans. R. Soc. London A: Math. Phys. Eng. Sci.* **240**(826), 599–642 (1948)

38. Muth, P., Wohlfarth, E.P. (eds.): *Ferromagnetic Materials*, vol. 3. North-Holland Publ. Co., Amsterdam (1983). 1982. *Crystal Research and Technology* 18 (9):1180-1180
39. De Bitetto, D.: Anisotropy fields in hexagonal ferrimagnetic oxides by ferrimagnetic resonance. *J. Appl. Phys.* **35**(12), 3482–3487 (1964)
40. Kazin, P., Trusov, L., Zaitsev, D., Tretyakov, Y.D., Jansen, M.: Formation of submicron-sized  $\text{SrFe}_{12-x}\text{Al}_x\text{O}_{19}$  with very high coercivity. *J. Magn. Magn. Mater.* **320**(6), 1068–1072 (2008)
41. Choi, D.H., Lee, S.W., An, S.Y., Park, S.-I., Shim, I.-B., Kim, C.S.: Mossbauer studies and magnetic properties of  $\text{BaFe}_{12-x}\text{Al}_x\text{O}_{19}$  grown by a wet chemical process. *IEEE Trans. Magn.* **39**(5), 2884–2886 (2003)
42. Buschow, K.H.J., Boer, F.R.: *Physics of Magnetism and Magnetic Materials*. Springer (2003)
43. Kittel, C.: Theory of the structure of ferromagnetic domains in films and small particles. *Phys. Rev.* **70**(11–12), 965 (1946)